











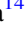





The Thermonuclear X-Ray Bursts of 4U 1730–22

Peter Bult^{1,2} , Giulio C. Mancuso^{3,4} , Tod E. Strohmayer⁵ , Arianna C. Albayati⁶ , Diego Altamirano⁶ ,
Douglas J. K. Buisson⁷ , Jérôme Chenevez⁸ , Sebastien Guillot⁹ , Tolga Güver^{10,11} , Wataru Iwakiri¹² ,
Gaurava K. Jaisawal⁸ , Mason Ng¹³ , Andrea Sanna¹⁴ , and Jean H. Swank² 

¹Department of Astronomy, University of Maryland, College Park, MD 20742, USA

²Astrophysics Science Division, NASA Goddard Space Flight Center, Greenbelt, MD 20771, USA

³Instituto Argentino de Radioastronomía (CCT-La Plata, CONICET; CICPBA), C.C. No. 5, 1894 Villa Elisa, Argentina

⁴Facultad de Ciencias Astronómicas y Geofísicas, Universidad Nacional de La Plata, Paseo del Bosque s/n, 1900 La Plata, Argentina

⁵Astrophysics Science Division and Joint Space-Science Institute, NASA's Goddard Space Flight Center, Greenbelt, MD 20771, USA

⁶Physics & Astronomy, University of Southampton, Southampton, Hampshire SO17 1BJ, UK

⁷Independent

⁸DTU Space, Technical University of Denmark, Elektrovej 327-328, DK-2800 Lyngby, Denmark

⁹Institut de Recherche en Astrophysique et Planétologie, UPS-OMP, CNRS, CNES, 9 avenue du Colonel Roche, BP 44346, F-31028 Toulouse Cedex 4, France

¹⁰Istanbul University, Science Faculty, Department of Astronomy and Space Sciences, Beyazit, 34119, Istanbul, Turkey

¹¹Istanbul University Observatory Research and Application Center, Istanbul University 34119, Istanbul, Turkey

¹²Department of Physics, Faculty of Science and Engineering, Chuo University, 1-13-27 Kasuga, Bunkyo-ku, Tokyo 112-8551, Japan

¹³MIT Kavli Institute for Astrophysics and Space Research, Massachusetts Institute of Technology, Cambridge, MA 02139, USA

¹⁴Dipartimento di Fisica, Università degli Studi di Cagliari, SP Monserrato-Sestu km 0.7, I-09042 Monserrato, Italy

Received 2022 September 19; revised 2022 October 14; accepted 2022 October 15; published 2022 November 23

Abstract

We present observations of the historic transient 4U 1730–22 as observed with the Neutron Star Interior Composition Explorer (NICER). After remaining in quiescence since its 1972 discovery, this X-ray binary showed renewed outburst activity in 2021 and 2022. We observed 4U 173–22 extensively with NICER, detecting a total of 17 thermonuclear X-ray bursts. From a spectroscopic analysis, we find that these X-ray bursts can be divided into a group of bright and weak bursts. All bright bursts showed 1–2 s rise times and a photospheric radius expansion phase, while the weak bursts showed a slower ~ 5 s rise with a tendency for concave shapes. From the photospheric radius expansion flux, we estimate the source distance at 6.9 ± 0.2 kpc. We consider various interpretations for our observations and suggest that they may be explained if accreted material is burning stably at the stellar equator and unstable ignition occurs at a range of higher latitudes.

Unified Astronomy Thesaurus concepts: [Low-mass x-ray binary stars \(939\)](#); [X-ray bursts \(1814\)](#)

1. Introduction

The low-mass X-ray binary 4U 1730–22 is a historic transient that was discovered in 1972 with the Uhuru satellite (Cominsky et al. 1978). After an outburst that lasted about 230 days (Chen et al. 1997), the source returned to quiescence and remained dormant for the subsequent 49 yr. Although 4U 1730–22 has been frequently cataloged as a possible neutron star X-ray binary (van Paradijs & White 1995; Chen et al. 1997), the first concrete evidence for this classification was presented by Tomsick et al. (2007). These authors identified the X-ray source CXOU J173357.5–220156 as a candidate quiescent X-ray counterpart to 4U 1730–22 using Chandra observations, finding that the quiescent spectrum was well described using a neutron star atmosphere model. Given a lack of further activity from this source, the association between 4U 1730–22 and the quiescent counterpart could not be confirmed. Beyond it being a candidate neutron star, very little was known about this source.

Renewed activity in the direction of 4U 1730–22 was detected with MAXI/GSC on 2021 June 7 (Kobayashi et al. 2021) and initially attributed to a new transient, tentatively dubbed MAXI J1733–222. Subsequent follow-up observations with Swift/XRT provided an improved source localization and

demonstrated that this outburst activity was in fact associated with 4U 1730–22 (Kennea et al. 2021a, 2021b). This association was later confirmed by the detection of an optical counterpart (Russell et al. 2021; Strader et al. 2021), whose precise location matches both the Swift localization and the quiescent source position of Tomsick et al. (2007).

After maintaining a relatively low X-ray flux of $\sim 10^{-10}$ erg s⁻¹ cm⁻² for a few weeks (Kennea et al. 2021a), the source started brightening substantially on July 5, reaching an order-of-magnitude increase in X-ray flux by July 6 (Iwakiri et al. 2021) as it transitioned from a hard to a soft accretion state. On July 7, the first thermonuclear (type I) X-ray burst from the source was detected with the Neutron Star Interior Composition Explorer (NICER; Bult et al. 2021), confirming that 4U 1730–22 indeed harbors an accreting neutron star. The intensity of the source gradually decayed over the subsequent ~ 100 days, although, for lack of pointed observations, it is unclear if and when 4U 1730–22 returned to quiescence.

On 2022 February 13, the MAXI Nova alert system (Negoro et al. 2016) again triggered on 4U 1730–22 as the source unexpectedly returned to a bright state. At this time, we began a regular monitoring campaign with NICER. We found that 4U 1730–22 remained in its bright soft state for about 150 days, only returning to a hard state in early 2022 July. Over the course of its prolonged soft-state phase, we detected 16 more X-ray bursts. An independent analysis of these data recently reported the detection of a 585 Hz burst oscillation in one of the X-ray bursts (Li et al. 2022).



Original content from this work may be used under the terms of the [Creative Commons Attribution 4.0 licence](#). Any further distribution of this work must maintain attribution to the author(s) and the title of the work, journal citation and DOI.

Table 1
X-Ray Burst Properties

No.	ObsID	MJD (TT)	PRE	Peak Flux ($\times 10^{-8}$ erg s $^{-1}$ cm $^{-2}$)	Fluence ($\times 10^{-7}$ erg cm $^{-2}$)	Rise (s)	τ (s)	ϵ_1 (s)	ϵ_2 (s)	α	t_{rec} (hr)
1	4202200125	59404.552433	N	4.9 ± 1.1	3.73 ± 0.08	5.4	7.6	...	8.2	512^{+154}_{-102}	
2	5202200101	59639.336264	N	6.5 ± 1.2	5.39 ± 0.11	3.6	8.2	...	9.5	339^{+102}_{-68}	
3	5202200112 ^a	59657.912770	Y	6.2 ± 0.6	$>5.80 \pm 0.09$	1.6	9.4	2.1	16.4	368^{+10}_{-74}	$>3.8 \pm 0.3$
4	5202200113	59658.960817	Y	7.7 ± 1.5	8.44 ± 0.10	2.1	11.0	1.9	15.1	251^{+75}_{-50}	5.6 ± 0.5
5	4639010102	59664.121513	Y	7.7 ± 1.4	9.58 ± 0.11	1.6	12.4	2.0	14.3	211^{+63}_{-42}	6.7 ± 0.6
6	4639010104	59666.949981	N	5.2 ± 0.9	3.85 ± 0.17	4.6	7.4	...	7.2	585^{+175}_{-117}	
7	4639010113	59675.595021	N	2.8 ± 0.4	2.92 ± 0.03	2.1	10.3	...	8.4	686^{+206}_{-137}	
8	4639010116	59678.770816	Y	7.0 ± 0.5	7.94 ± 0.10	1.6	11.4	2.3	14.9	227^{+68}_{-45}	6.2 ± 0.5
9	4639010131	59695.093117	Y	7.5 ± 0.7	6.79 ± 0.08	1.1	9.1	2.1	13.5	230^{+69}_{-46}	6.1 ± 0.5
10	4639010141	59718.325513	Y	6.2 ± 0.5	7.63 ± 0.10	1.1	12.3	3.4	13.7	200^{+60}_{-40}	7.1 ± 0.6
11	4639010146	59723.819599	N	4.5 ± 0.9	3.73 ± 0.07	5.6	8.2	...	9.0	457^{+137}_{-91}	
12	4639010160	59739.423071	Y	7.0 ± 1.0	6.89 ± 0.08	1.1	9.9	2.8	13.4	189^{+57}_{-38}	7.5 ± 0.6
13	4639010160	59739.868686	Y	8.1 ± 1.0	8.22 ± 0.09	1.1	10.1	2.1	13.9	132^{+39}_{-26}	10.7 ± 0.9
14	4639010166	59747.677906	Y	6.7 ± 0.4	9.26 ± 0.11	1.6	13.9	2.3	14.8	162^{+49}_{-32}	8.7 ± 0.7
15	4639010175	59756.854948	Y	6.5 ± 1.5	9.04 ± 0.09	1.9	14.0	2.9	14.9	100^{+30}_{-20}	14.0 ± 1.2
16	4639010177 ^{a,b}	59760.004202	Y	5.3 ± 0.6	$>5.20 \pm 0.06$	1.4	9.8	4.4	10.0	194^{+38}_{-39}	$>7.3 \pm 0.6$
17	4639010179	59762.731650	Y	7.1 ± 1.3	8.89 ± 0.24	2.4	12.5	2.4	17.2	98^{+20}_{-20}	14.4 ± 1.2

Notes. The MJD column lists the onset time of the burst. The “PRE” column indicates whether the burst exhibited PRE (Y) or not (N). The peak flux and fluence are both bolometric. The “Rise” column gives the rise time of the bursts, while ϵ_1 and ϵ_2 give the e-folding timescales (see Section 3.1). The α column (see Equation (1)) was calculated assuming a burst recurrence time of 10 hr, whereas the t_{rec} column gives the recurrence time if we instead assume $\alpha = 140$ (see Section 4.1 for a discussion of these columns). Uncertainties are quoted at 68% confidence.

^a Truncated by the end of the observation.

^b Burst detected during SAA.

In this paper, we combine the 2021 and 2022 NICER observations of 4U 1730–22 to present a detailed spectroscopic analysis of all detected X-ray bursts from this source.

2. Observations

We observed 4U 1730–22 with NICER in 2021 and 2022 for a total unfiltered exposure of 102 and 574 ks, respectively. These observations are collected under ObsIDs starting with 420220, 463901, and 520220. We processed the data using NICERDAS version 9, as distributed with HEASOFT version 6.30. All standard filter criteria were applied, meaning that we retained only those epochs during which the pointing offset was $<54''$, the Earth elevation angle was $>15^\circ$, the elevation angle with respect to the bright Earth limb was $>30^\circ$, and the instrument was not in the South Atlantic Anomaly (SAA). Additionally, we applied standard background filter criteria; we removed all epochs during which the rate of detected reset triggers per detector (undershoots) is larger than $500 \text{ counts s}^{-1}$ or when the rate of high-energy events per detector (overshoots) is either greater than 1.5 or greater than $1.5 \times \text{COR_SAX}^{-0.633}$, where COR_SAX gives the geomagnetic cutoff rigidity in units of GeV c^{-1} . To prevent the overshoot filters from introducing spurious 1–10 s gaps in the data, we followed Bult et al. (2020) and applied a 5 s window smoothing to the overshoot rates prior to evaluating the filter condition. Finally, we added the requirement that all 52 detectors were active during the observation.

The filter criteria described above yielded clean data products for the vast majority of ObsIDs analyzed in this paper. However, in 21 ObsIDs, we found periods of low-level background flaring related to polar horn passages (Remillard et al. 2022) that were not fully removed. For these ObsIDs, we removed the epochs during which the cutoff rigidity

(COR_SAX) was smaller than 1.5 GeV c^{-1} . In all cases, this appropriately removed the background-dominated epochs.

After processing, we were left with 72 and 430 ks clean exposure for the 2021 and 2022 outbursts, respectively. Visually inspecting the light curves of these data, we identified 16 thermonuclear (type I) X-ray bursts. Comparing to the unfiltered light curve, we identified one additional X-ray burst during an SAA passage. Because the background was only modestly elevated during the SAA passage in which this additional X-ray burst was detected, we included this epoch in our analysis. The ObsIDs and occurrence times of these bursts are reported in Table 1.

3. Results

3.1. Light Curves

We group the data by continuous pointing. We find that there are 607 such pointings in the data set, with exposures ranging from 150 to 2500 s. For each pointing, we calculate the average count rate in the 0.5–10 keV energy band, as well as a hardness ratio defined as the 3–10 keV rate over the 0.5–1.5 keV rate. The resulting light curve and hardness evolution are shown in Figure 1. We see that our observations sample the source in two states: a fainter hard state at count rates of $\approx 50 \text{ counts s}^{-1}$ and a brighter soft state with count rates $\gtrsim 250 \text{ counts s}^{-1}$. All X-ray bursts were detected in the soft state.

The X-ray burst light curves show most of their flux during the first ≈ 20 s, but they show long low-intensity tails, taking about 100 s for the burst count rate to return to the preburst level. In spite of the long tail, we observed the entire X-ray burst in all cases except bursts 3 and 16. For these two bursts, the tail was truncated by the end of the observation at >30 s after onset. In Figure 2, we show the light curves of the 17

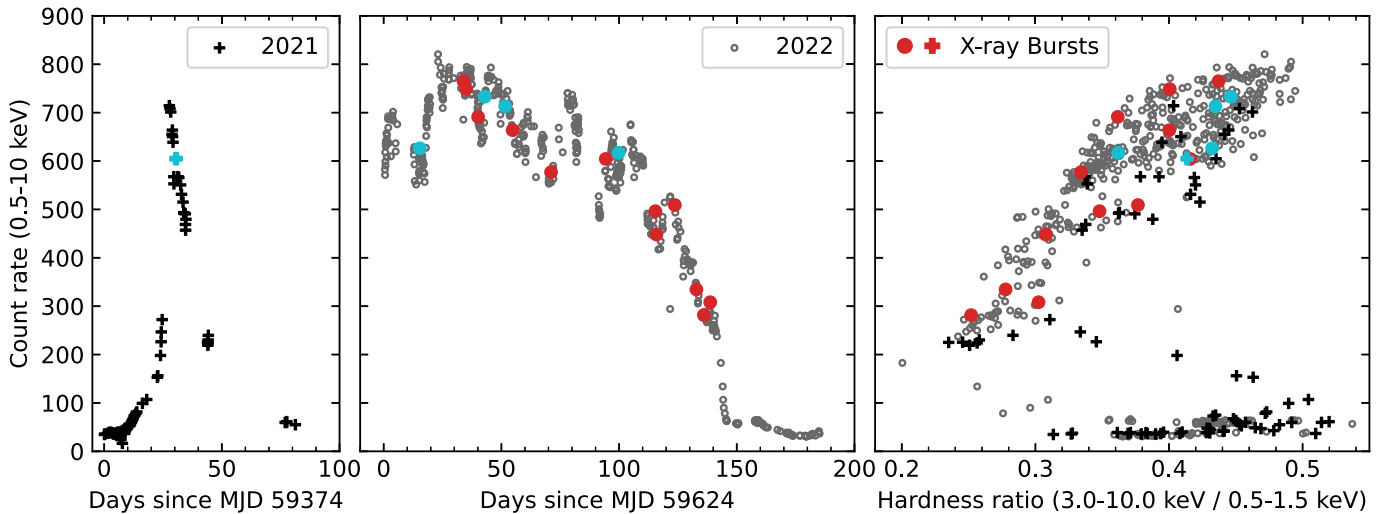


Figure 1. Light curves in the 0.5–10 keV band (left and middle) and hardness intensity diagram (right) of 4U 1730–22, with each point representing a single NICER pointing. Those pointings containing an X-ray burst are marked in teal (weak) and red (bright).

observed X-ray bursts in the 0.5–10 (black line) and 4–10 (gray area) keV bands. Based on the morphology of their preburst rate subtracted profiles, we can divide the bursts into two categories: a weak and a bright group.

The group of weak bursts is characterized by slow rise times of about 5 s and peak count rates on the order of 2000 counts s^{-1} . The group of bright bursts show a more rapid rise, taking about 1–2 s to reach peak count rates between 6000 and 8000 counts s^{-1} . These brighter bursts then consistently show an initial sharp decline in count rate back to 2000 counts s^{-1} . From that point on, the burst decay transitions into a slower trend that is similar to the decays seen in the weak bursts. Further, we note that a number of the bright bursts show a temporary plateau at 2000 counts s^{-1} before continuing their decay. See, for instance, bursts 5 and 17 in Figure 2. The initial fast rise and rapid decay of the bright group suggests that the ignition of these bursts occurs in a hydrogen-poor environment, while the much slower rise of the weak group instead points to ignition in a hydrogen-rich environment (Galloway & Keek 2021).

It is clear that for both weak and bright bursts, the 2000 counts s^{-1} rate signifies some special state in the burst evolution. Another aspect of this behavior is that the inflection in the tail of the bright bursts consistently occurs about 5 s after onset. This aligns with the time it takes for the weak bursts to reach their peak intensity. This phenomenon is illustrated in the bottom right panel of Figure 2, where we plot bursts 5 and 6 together.

Looking closer at the group of bright bursts, we also note that the initial peak is less pronounced in the 4–10 keV light curves. Hence, this peak appears to be predominantly driven by softer photons, suggesting the presence of a photospheric radius expansion (PRE) phase. Further, by comparing the different burst profiles (bottom row of Figure 2), we see that while many of these bursts have generally similar peak rates, some bursts are notably brighter (5, 9, 13, and 15), while 2 and 16 fall somewhere in between the two groups.

To quantify the burst shapes, we define the burst rise time as the time it takes from the onset to reach peak intensity, with the onset determined visually to optimize the alignment between the bursts. For each burst, we also attempted to measure the exponential decay timescale. Because an exponential function

is unable to account for the break observed in the bright bursts, we split the burst tails into phases. For each of the bright bursts, we measure the exponential decay timescale, ϵ_1 , between $[t_0 + 2 \text{ s}, t_0 + 5 \text{ s}]$, where t_0 is the respective burst onset time. For both the faint and bright bursts, we measure a second decay timescale between $[t_0 + 5 \text{ s}, t_0 + 30 \text{ s}]$, which we call ϵ_2 . The rise times and exponential decay timescales are reported in Table 1.

3.2. Time-resolved Spectroscopy

We perform a spectroscopic analysis of each of the observed X-ray bursts using XSPEC v12.12.1c (Arnaud 1996). The interstellar absorption is modeled using the Tübingen–Boulder model (Wilms et al. 2000). Background spectra were generated using the NICER 3C 50 model (Remillard et al. 2022). All X-ray spectra were binned using the optimal binning method of Kaastra & Bleeker (2016), additionally requiring at least 25 events per spectral channel.

We begin by considering the spectrum of the persistent (nonburst) emission around the time each X-ray burst was observed. We extracted a preburst spectrum in the 0.5–10 keV range from the epoch $[t_0 - 225 \text{ s}, t_0 - 25 \text{ s}]$, where t_0 refers to the respective burst onset time. We model these preburst spectra using an absorbed multitemperature disk blackbody (`diskbb`; Mitsuda et al. 1984; Makishima et al. 1986) plus a thermally Comptonized continuum (`nthcomp`; Zdziarski et al. 1996; Życki & Done 1999), which yields a reasonably good description of the continuum emission in all cases. We further use the `cflux` model component to estimate the unabsorbed bolometric flux by extrapolating our model over the 0.01–100 keV energy range. We find a consistent absorption column density across all preburst spectra, with a mean value of $N_H = (7.1 \pm 0.3) \times 10^{21} \text{ cm}^{-2}$. Considering the preburst spectra as a function of flux, we observe an evolution in the disk component, which increases in temperature from about 0.8 to 1.8 keV. The photon index remains constant in all spectra, with an average value of 2.0 ± 0.1 , while the Comptonization normalization increases from 0.2 to 0.4 photons $\text{keV}^{-1} \text{ cm}^{-2} \text{ s}^{-1}$ at 1 keV. The detailed best-fit parameters are listed in Table 2.

To analyze the emission of the X-ray bursts themselves, we extracted the burst epochs between $[t_0 - 5 \text{ s}, t_0 + 95 \text{ s}]$, using

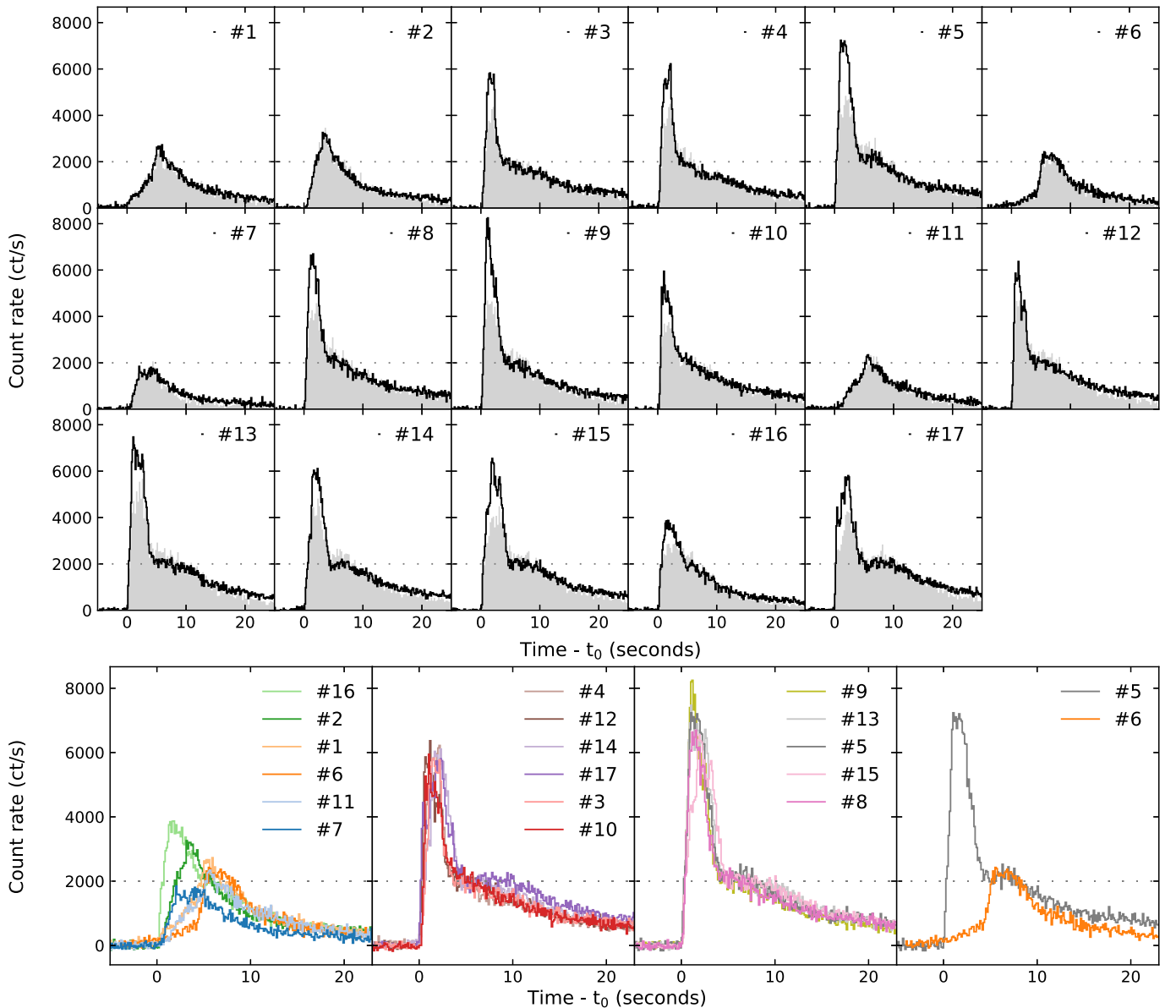


Figure 2. Light-curve profiles of the 17 X-ray bursts observed from 4U 1730–22. The top panels show the individual bursts as labeled, with the black line showing the 0.5–10 keV count rate at 1/8 s time resolution and the gray area showing the 4–10 keV count rate (1/4 s resolution, multiplied by a factor of 4). The four panels in the bottom row show various groupings of bursts for comparison, with both labels and color coding ordered by increasing peak count rate. All curves are plotted relative to their respective burst onset time (Table 1) and with the preburst count rate subtracted. Additionally, a horizontal dotted line was added to each panel at 2000 counts s^{-1} to guide the eye.

all events in the 0.5–10 keV energy range. We then proceeded to dynamically bin the X-ray burst data such that each bin contained 2000 events. The time-resolved burst spectra were extracted from these dynamic bins.

We initially modeled the burst spectra using a simple absorbed blackbody model. That is, we added a blackbody component to the respective preburst model and fixed all model parameters but the blackbody normalization and temperature. This approach yielded a very poor description of the data. The best-fit reduced χ^2 scores were found to increase with the source count rate, peaking at scores of 3–5 (with associated p -values of $<10^{-13}$) around the times of peak burst count rates.

In a second approach we rescaled the preburst model component using a variable factor, f_a (Worpel et al. 2013, 2015). This approach greatly improved the model fits, yielding acceptable χ^2 scores throughout each of the bursts. In Figure 3,

we show an example spectrum comparing the blackbody model to the f_a model fit, while in Figure 4, we show the resulting time-resolved spectroscopic evolution for a few example bursts. We find that measured f_a values roughly follow the burst light curves, peaking at values of about 3 for the group of weak bursts, while the group of bright bursts show f_a values as high as 10. Key burst parameters are listed in Table 1.

Each of the X-ray bursts in the bright group shows PRE; the blackbody temperature dips and then rises, while simultaneously, the blackbody normalization peaks and then decays. Notably, we find that “touchdown” (the time at which the blackbody peaks in temperature) occurs at $t_0 + 5$ s, the same time at which these bright bursts show an inflection in their light curves.

For each modeled burst spectrum, we calculate the bolometric flux contributed by the blackbody. We further estimate

Table 2
Preburst Spectroscopy

No.	N_{H} ($\times 10^{21} \text{ cm}^{-2}$)	T_{in} (keV)	diskbb Norm.	Photon Index	nthcomp Norm.	Flux ($\times 10^{-9} \text{ erg s}^{-1} \text{ cm}^{-2}$)	χ^2/dof
1	6.9 ± 0.2	$1.48^{+0.09}_{-0.10}$	$12.0^{+3.5}_{-2.0}$	1.93 ± 0.10	0.30 ± 0.03	5.3 ± 0.2	139.1/113
2	7.1 ± 0.2	$1.74^{+0.10}_{-0.12}$	$7.5^{+1.5}_{-1.1}$	$2.05^{+0.17}_{-0.13}$	0.34 ± 0.03	$5.1^{+0.6}_{-0.3}$	120.6/108
3	7.2 ± 0.2	$1.57^{+0.10}_{-0.09}$	13^{+3}_{-2}	$1.94^{+0.12}_{-0.08}$	0.41 ± 0.03	$5.9^{+0.5}_{-0.2}$	157.0/117
4	7.1 ± 0.2	$1.37^{+0.10}_{-0.11}$	18^{+7}_{-3}	1.95 ± 0.10	$0.41^{+0.04}_{-0.05}$	$5.9^{+0.5}_{-0.3}$	170.9/114
5	7.4 ± 0.2	$1.23^{+0.10}_{-0.08}$	21^{+6}_{-5}	$2.00^{+0.08}_{-0.06}$	$0.43^{+0.03}_{-0.04}$	$5.6^{+0.4}_{-0.3}$	158.5/112
6	7.4 ± 0.2	$1.79^{+0.07}_{-0.11}$	$8.8^{+1.3}_{-1.0}$	$2.12^{+0.19}_{-0.15}$	0.40 ± 0.03	$6.2^{+1.0}_{-0.6}$	171.8/115
7	7.1 ± 0.2	$1.61^{+0.13}_{-0.14}$	$10.0^{+3.5}_{-1.8}$	$1.96^{+0.14}_{-0.10}$	$0.39^{+0.02}_{-0.03}$	5.6 ± 0.4	166.1/115
8	7.1 ± 0.2	$1.34^{+0.10}_{-0.09}$	16^{+5}_{-4}	1.92 ± 0.08	0.37 ± 0.04	$5.0^{+0.7}_{-0.2}$	138.8/114
9	7.1 ± 0.3	$1.10^{+0.09}_{-0.08}$	28^{+11}_{-8}	$1.96^{+0.09}_{-0.10}$	0.33 ± 0.04	4.3 ± 0.3	135.3/110
10	6.9 ± 0.3	$1.26^{+0.10}_{-0.09}$	18^{+7}_{-5}	$1.81^{+0.09}_{-0.10}$	0.30 ± 0.04	$4.2^{+0.3}_{-0.2}$	153.5/114
11	7.0 ± 0.2	$1.31^{+0.12}_{-0.08}$	17 ± 4	$1.95^{+0.10}_{-0.07}$	0.36 ± 0.03	$4.7^{+0.5}_{-0.4}$	95.2/112
12	7.0 ± 0.3	$1.08^{+0.11}_{-0.06}$	24 ± 8	$1.86^{+0.10}_{-0.08}$	0.28 ± 0.04	$3.6^{+0.4}_{-0.3}$	182.6/109
13	6.7 ± 0.3	$0.88^{+0.05}_{-0.04}$	54^{+17}_{-16}	$1.81^{+0.12}_{-0.13}$	$0.21^{+0.05}_{-0.04}$	$3.00^{+0.34}_{-0.15}$	116.5/108
14	7.2 ± 0.2	$1.33^{+0.15}_{-0.12}$	10^{+4}_{-3}	$1.95^{+0.09}_{-0.07}$	0.33 ± 0.03	$4.2^{+0.4}_{-0.2}$	170.4/111
15	7.0 ± 0.3	0.78 ± 0.06	48^{+25}_{-18}	$1.93^{+0.10}_{-0.12}$	0.21 ± 0.04	$2.52^{+0.43}_{-0.10}$	109.8/102
16	$7.4^{+0.3}_{-0.4}$	0.82 ± 0.09	28^{+21}_{-12}	$2.16^{+0.09}_{-0.12}$	$0.23^{+0.03}_{-0.04}$	$2.8^{+0.4}_{-0.3}$	133.3/ 99
17	$7.1^{+0.3}_{-0.4}$	$0.80^{+0.14}_{-0.11}$	31^{+31}_{-16}	$1.89^{+0.09}_{-0.11}$	0.21 ± 0.03	2.4 ± 0.3	97.0/104

Note. We report the unabsorbed bolometric flux. Uncertainties are quoted at 90% confidence.

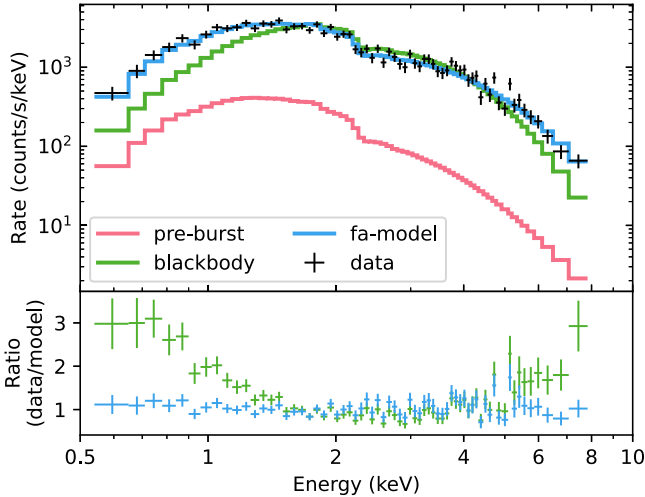


Figure 3. Best-fit spectra of burst 5 at peak intensity, showing, in the top panel, the measured spectrum (black), the preburst model (red), a blackbody model (green), and the fa-model (blue). The bottom panel gives the ratio of the data over the respective models. Note that the spectral bin above 8 keV had an insufficient event count and was removed from the fit.

the burst flux that is not captured by the blackbody as $(f_a - 1) \times F_{\text{preburst}}$, where F_{preburst} is the bolometric flux measured for the respective preburst spectrum (Table 2). Finally, we define the total burst flux as the sum of the blackbody and secondary emission components.

Considering the evolution of the flux over time, we find that the blackbody flux systematically drops during the PRE phase, while the total burst flux remains constant in time. This pattern is illustrated in Figure 5, where we show the bolometric flux of these two components as a function of blackbody temperature. The upper branch of the track represents the PRE phase, moving toward the right as the photosphere expands in radius. The flux contributed by the blackbody (black points) decreases with radius, while the total burst flux (red points) remains constant. We therefore adopt the total

burst flux as the more accurate measure for the burst energy. To estimate the PRE flux, we average all burst flux measurements during the PRE phase of the bursts that show one, which gives us $F_{\text{PRE}} = (6.75 \pm 0.25) \times 10^{-8} \text{ erg s}^{-1} \text{ cm}^{-2}$.

4. Discussion

We have presented a spectroscopic analysis of 17 thermonuclear X-ray bursts observed from 4U 1730–22 with NICER. We found that the burst light curves can be divided into two groups: slow-rising weak bursts and fast-rising bright bursts. We observed PRE in each of the bright bursts and estimated the bolometric burst flux during the PRE phase to be $F_{\text{PRE}} = (6.75 \pm 0.25) \times 10^{-8} \text{ erg s}^{-1} \text{ cm}^{-2}$. Equating this flux to the $3.8 \times 10^{38} \text{ erg s}^{-1}$ empirical Eddington luminosity of Kuulkers et al. (2003), we obtain a source distance estimate of $6.9 \pm 0.2 \text{ kpc}$. An important caveat to this distance estimate is that we choose to use the total burst flux to estimate the PRE flux (see Section 4.2 for further discussion on this point). If we instead use the blackbody contribution only, then the PRE flux is about 15% smaller and the estimated distance 0.5 kpc larger. We consider this offset a systematic uncertainty.

Using our estimated distance, we calculate the source luminosity for each of the preburst spectra reported in Table 2. We find values ranging from 1.4×10^{37} to $3.5 \times 10^{37} \text{ erg s}^{-1}$, which amounts to 4%–10% of the Eddington luminosity.

4.1. Burst Phenomenology

The X-ray bursts of 4U 1730–22 show a rather interesting phenomenology. Based on the light curves shown in Figure 2, we can think of the bright bursts as a superposition of two components. Over the first 5 s, the bursts show a “fast” component: the count rate rises quickly and stabilizes for a second or two before dropping back down. At about 5 s after onset, the burst profile becomes dominated by a second “slow” component, which causes a shoulder in the light curve before continuing as a slower decay. The weak bursts can then be

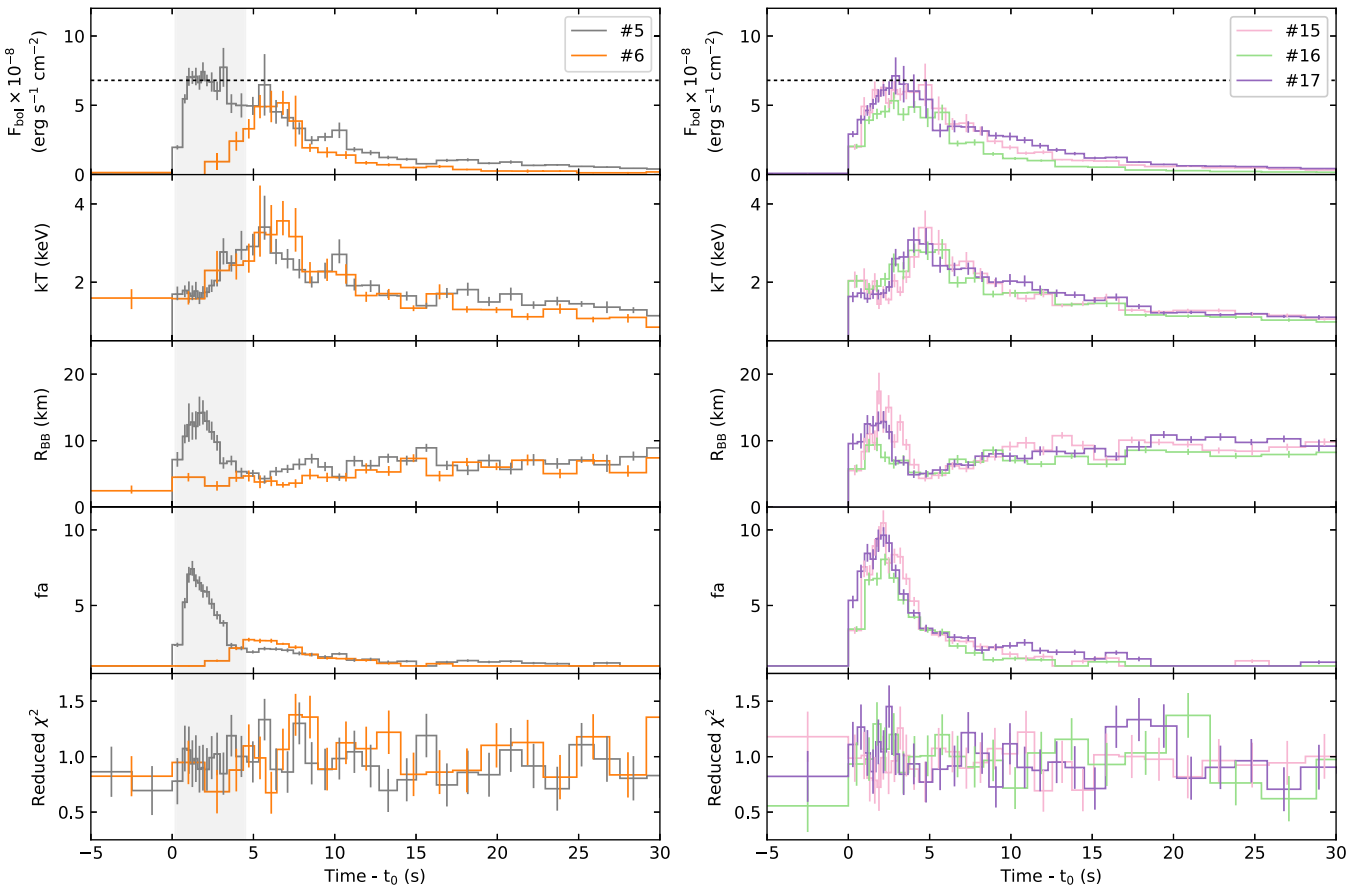


Figure 4. Time-resolved spectroscopy of bursts 5 (left, gray), 6 (left, orange), 15 (right, pink), 16 (right, green), and 17 (right, purple), using the same color coding as in Figure 2. Both panels show, from top to bottom, the bolometric burst flux, blackbody temperature, blackbody radius (at 6.9 kpc), f_a factor, and reduced χ^2 . We further highlighted the epoch of radius expansion for burst 5 in the left panel. The error bars show 1σ uncertainties, which for the bottom panels were calculated as $\sqrt{2/\text{dof}}$, with dof the degrees of freedom. The dashed line in the top panels indicates the PRE flux.

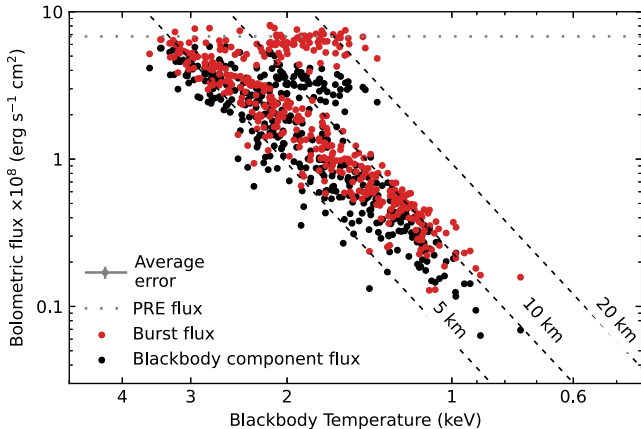


Figure 5. Flux temperature diagram for the X-ray bursts of 4U 1730–22. The bolometric flux contributed by the blackbody component is shown in black, while the red points show the bolometric flux of the whole burst spectrum (blackbody plus the excess but not including the preburst contribution; see text). The horizontal dotted line indicates the PRE flux, while the three diagonal dashed lines show the constant radius contours as labeled, assuming a source distance of 6.9 kpc. These contours are for illustrative purposes only, as they do not take color corrections into account (see, e.g., Suleimanov et al. 2017). Error bars were omitted for clarity, but see the gray point in the legend for the average scale of the uncertainty.

interpreted as showing only the second “slow” component (see Figure 2).

All X-ray bursts were detected while 4U 1730–22 was in the soft state; hence, the difference between the weak and bright

types is not related to the accretion state in any obvious way. Even when accounting for variations of the intensity and hardness ratio within the soft state (Figure 1), we find that either burst type can occur for the same conditions. The only evident difference is that the weak bursts tend to occur at higher (persistent) intensities, generally while the source flux is above $\approx 5 \times 10^{-9} \text{ erg s}^{-1} \text{ cm}^{-2}$ (see Table 2), or about 7.5% of the Eddington luminosity. We caution against overinterpreting this finding, however, as the bright bursts are the more common burst type. Hence, the nondetection of weak bursts at lower intensities may simply be a sampling artifact.

From our spectroscopic analysis, we found that the “fast” component of the bright bursts is associated with a PRE phase. Indeed, none of the weak bursts show evidence for PRE, although we note that many still reach fluxes near the Eddington limit. Two additional features emerge when we compare the time-resolved spectroscopy of the different types of bursts. First, the time at which the PRE phase ends and the photosphere settles back on the stellar surface coincides with the time at which the weak bursts reach their peak flux. Second, the blackbody temperature shows the same time evolution in all X-ray bursts.

It is tempting to associate the “fast” and “slow” components of the light curve directly with the nuclear processes that power an X-ray burst. The “fast” component, with its fast evolution and high luminosity, has the hallmarks of helium burning and, if seen in isolation, would be interpreted as a pure helium burst (Fujimoto et al. 1981; Narayan & Heyl 2003). By comparison,

the “slow” component could then be attributed to hydrogen burning via the rapid-proton (rp) capture reaction chain (Wallace & Woosley 1981; Schatz et al. 2001), which tends to proceed much more slowly. The difference between the weak and bright bursts is one of ignition depth, with the bright bursts being due to ignition in a deep layer of pure helium, while the weak bursts are due to ignition in a shallower layer containing hydrogen. While this picture may explain some of the basic systematics we observe, there are more subtle effects in our data that deserve attention.

4.1.1. Burst Energy and Recurrence

First, let us point out that both bright and weak bursts have similar timescales of about 10–15 s. This is still much shorter than the 20–40 s typically seen for bursts with a high hydrogen abundance (the most notable example being GS 1826–24; Galloway et al. 2008, 2020). Hence, if some hydrogen is present in the burst fuel, its abundance is probably modest and not too dissimilar between the two kinds of bursts. Optical observations of 4U 1730–22 have detected strong hydrogen and weak helium emission lines (Strader et al. 2021), indicating that the accreting matter is likely hydrogen-rich. Given that the burst profiles do not reflect this abundance, it seems likely that hydrogen is burning stably between bursts through the hot CNO cycle.

The duty cycle at which we sampled 4U 1730–22 is, on average, about 4%. Given this comparatively sparse coverage, we cannot reliably determine the waiting time between individual bursts. As a first-order estimate of the average burst recurrence, however, we could assume that the bursts occurred at a roughly constant rate and divide the total collected exposure by the number of observed bursts. Taking the 2022 data, which contain all but one of our bursts, we have an unfiltered exposure of 574 ks, giving $t_{\text{recurrence}} = 10^{+3}_{-2}$ hr, with the uncertainties following from Poisson counting statistics. For comparison, the shortest waiting time between observed bursts was 10.9 hr for bursts 12 and 13, suggesting that the average recurrence is reasonably accurate at later times in the outburst.

If we adopt the average recurrence time of 10 hr, we can calculate the implied α ratio for each observed burst as (Gottwald et al. 1986; Galloway et al. 2008)

$$\alpha = \frac{F_{\text{preburst}} \Delta t_{\text{recurrence}}}{E_{\text{burst}}}, \quad (1)$$

with the resulting values listed in Table 1. If we further assume that each X-ray burst burns through all accreted matter, then the theoretically expected α is ≈ 40 for hydrogen-rich X-ray bursts and 100–150 for pure helium bursts (Galloway et al. 2008). For some of the later bursts, this assumed recurrence time is compatible with a burst that is mostly due to helium (12 and up), as expected from the burst profiles. For the earlier bursts, however, the estimated values for α are unreasonably high. In particular, the weak bursts exceed nominal α values by a factor of 4–5, while the bright bursts have a more modest factor of 2–3 excess. This suggests that either the recurrence time was much shorter for the earlier X-ray bursts, not all matter accreted between bursts contributes to the burst fluence, or both.

Traditional 1D theoretical models of burst ignition predict that the burst rate should increase with mass accretion rate (Fujimoto et al. 1981; Narayan & Heyl 2003). Hence, the higher accretion rate of the earlier bursts could well mean that

these bursts had recurrence times much shorter than our assumed 10 hr. If we assume that bursts 12 and 13 are indeed consecutive bursts, then their recurrence time gives us $\alpha = 140 \pm 12$. By adopting this measured α for all bright bursts, we can use Equation (1) to calculate the implied recurrence times. We find that these recurrence times span 5.6–14.4 hr (see Table 1). There is an issue with the lower bound of these burst recurrence times, however; it does not leave enough time for the CNO cycle to reduce the hydrogen fraction in the accretion column. For solar abundances, it takes approximately 10 hr for the CNO cycle to deplete hydrogen at the base of the accretion column (Lampe et al. 2016). Hence, if the implied recurrence times were correct, then we would expect the hydrogen abundance in these bursts to be changing as well. Yet such a change in abundance is not apparent in the burst profiles.

In practice, there is another issue to consider: the relation between the mass accretion rate and the burst recurrence does not always hold. At a sufficiently high mass accretion rate, the burst rate is observed to decrease (Cornelisse et al. 2003; Galloway et al. 2008). Additionally, the critical accretion rate at which that turnover occurs is a function of the stellar spin frequency (Galloway et al. 2018; Cavecchi et al. 2020). For 4U 1730–22, with a presumed spin frequency of 585 Hz (Li et al. 2022), the burst rate likely peaks around 5% Eddington (Cavecchi et al. 2020). Hence, we would expect the burst rate to decrease as the mass accretion rate goes up, which is opposite to the trend needed to explain our results.

One way our data might be reconciled with theory is if the 585 Hz burst oscillation reported by Li et al. (2022) does not correspond to the neutron star spin frequency. While the high signal strength of this oscillation makes it unlikely that it was a spurious detection, we note that the oscillation was only significant for about 1 s. This is a much shorter signal duration than normally seen for burst oscillations (Watts 2012; Bilous & Watts 2019), even in the NICER band (Bult et al. 2019). Hence, there remains a possibility that the oscillation reported by Li et al. (2022) is what Bilous & Watts (2019) called a “glimmer” and that it is unrelated to the neutron star spin frequency.

4.1.2. Ignition Latitude

The more likely interpretation of our data is that not all accreted matter burns in the X-ray burst. If some part of the accreted envelope is not involved in the X-ray burst, then the α estimated through Equation (1) will overestimate the α predicted from theory. One way this might happen is if the formation of a boundary layer concentrates accretion onto the stellar surface in the equatorial region (Inogamov & Sunyaev 1999; Spitkovsky et al. 2002). The local accretion rate at the equator could then be high enough to support stable burning of both hydrogen and helium while still allowing unstable helium ignition at higher latitudes (Cavecchi et al. 2017).

There are several features in 4U 1730–22 that appear to support the idea of a boundary layer causing equatorial stable burning. The first is the fact that the weak bursts tend to have a slow rise with a tendency toward a concave shape. Such a concave burst rise has been argued to be a signature of burst ignition near the stellar poles (Maurer & Watts 2008). Because both the ignition conditions and the flame spreading speed should depend on latitude (Spitkovsky et al. 2002; Cooper & Narayan 2007), this could then also naturally explain the

difference between weak and bright bursts, with the former originating near the poles and the latter occurring at less extreme latitudes. A second relevant observation is that 4U 1730–22 is a prominent source of millihertz quasi-periodic oscillations (QPOs; G. C. Mancuso et al. 2022, in preparation). Such millihertz QPOs are generally believed to be due to marginally stable burning (Heger et al. 2007; Altamirano et al. 2008) and may arise naturally at the boundaries of a stable burning region around the equator (Cavecchi et al. 2020). Finally, a third effect comes from the excess flux in the burst spectrum, which again points to the presence of a boundary layer. We discuss this point in Section 4.2.

4.1.3. Short Recurrence Bursts

Finally, as an alternative explanation for the weak bursts, we consider the possibility that they are short time recurrence bursts: X-ray bursts that occur within a few minutes to at most half an hour after the previous event (Boirin et al. 2007; Keek et al. 2010). Such short recurrence bursts are not due to the accumulation of a fresh accretion column but rather thought to be caused by the turbulent mixing bringing unburned material from the previous burst down to ignition depth. Observationally, such events are often observed as a train of X-ray bursts that tend to become progressively weaker. Hence, the weak bursts of 4U 1730–22 could be interpreted as one of the later events of such a short recurrence train. While we did not observe any such short recurrence burst trains, the low duty cycle of our sampling means that we cannot rule them out either. Typically, our observations span only about ~ 1000 s around an observed X-ray burst, leaving room for recurrences of $\gtrsim 10$ minutes. More importantly, however, Keek et al. (2010) found that short recurrence bursts tend to be cooler than the primary burst and lack the slower decay component due to the rp process. This phenomenon is believed to be due to the fact that these short recurrence events occur in a hydrogen-depleted environment. The weak bursts of 4U 1730–22 do not exhibit this behavior. While the fluence of the weak bursts is lower, their peak flux, temperature evolution, and duration are more or less the same as for the bright bursts. Hence, the weak bursts are likely not short recurrence time events.

4.2. The Enhanced Burst Emission

All X-ray bursts observed from 4U 1730–22 showed a significant departure from a pure thermal spectrum. We accounted for the excess flux in X-ray burst emission by using the f_a model of Worpel et al. (2013). The measured values of f_a were found to roughly correlate with the burst intensity. The weak bursts had peak f_a values of about 2–3, while the bright PRE bursts showed peak f_a values between 7 and 10. These results are similar to those found with RXTE (Worpel et al. 2013, 2015), as well as more recent studies with NICER (Güver et al. 2022a, 2022b). A more subtle effect apparent in our observations is that the X-ray bursts observed at later times appear to have higher peak f_a values. That is, PRE bursts observed when the persistent intensity is high tend to peak at values of about 7, while the later time X-ray bursts (notably, 16 and 17) reach much higher values of about 10. This pattern suggests that the magnitude of the flux excess depends not only on the intensity of the thermal burst emission but also on the mass accretion rate (or, perhaps more appropriately, the accretion state).

The detection of excess burst emission has become increasingly common in recent years, either through the increased sensitivity afforded by NICER (Keek et al. 2018a, 2018b; Bult et al. 2019; Jaisawal et al. 2019; Güver et al. 2022a, 2022b) or through broadband X-ray coverage with AstroSat (Bhattacharyya et al. 2018; Roy et al. 2021; Kashyap et al. 2022) or Insight-HXMT (Chen et al. 2019). While the emission of a neutron star atmosphere is expected to deviate from Planck’s law (London et al. 1986; Madej et al. 2004; Suleimanov et al. 2011), the observed deviations from a blackbody spectrum are well in excess of what an atmosphere model can explain (in’t Zand et al. 2017). Instead, this flux excess is understood to be an indicator of interactions between the burst emission and the accretion flow surrounding the neutron star (Degenaar et al. 2018), even if the precise nature of that interaction remains a topic of investigation. Of the various interactions that can take place, three processes are commonly considered to explain the excess flux. First, the burst emission is reprocessed in the surface layers of the accretion disk and “reflected” back into the line of sight (Ballantyne 2004; Ballantyne & Strohmayer 2004), thereby adding a secondary reflection component to the spectrum, whose magnitude should approximately follow the burst intensity. Second, the burst radiation could induce a Poynting–Robertson (PR) drag in the inner accretion disk (Walker & Meszaros 1989; Walker 1992), which temporarily increases the accretion rate onto the stellar surface. Third, the stellar surface could be covered by a boundary layer, such that our view of the neutron star is (partially) obscured by a Comptonizing medium (Kajava et al. 2014; Koljonen et al. 2016).

Given the uncertainty about its origin, the presence of a flux excess makes it more challenging to discern how much of the observed X-ray emission is directly due to the thermonuclear processes in the stellar envelope and how much is added by the interaction with the accretion disk. In our analysis, we therefore calculated both the total flux in the X-ray burst (minus the preburst contribution) and the blackbody contribution separately. As shown in Figure 5, we found that the flux of the blackbody component decreases during the PRE phase, while the total burst flux remains constant. We take this to mean that it is the total burst flux that corresponds to the Eddington luminosity, which implies that the deviation away from pure blackbody emission is due to a (Comptonizing) scattering medium that (partially) obscures the line of sight to the neutron star. This behavior is naturally explained by the boundary layer interpretation. The disk reflection and PR drag mechanisms cannot be entirely ruled out, though. Numerical simulations of the disk response to the X-ray burst radiation suggest that both reflection and PR drag can occur simultaneously and act to increase the scale height of the X-ray burst (Fragile et al. 2020). Depending on the resulting height of the disk and the binary inclination of 4U 1730–22, it is possible that the inflated disk temporarily obscures the neutron star.

In this context, it is worth asking how much of the total observed flux is contributed by either the blackbody or the nonthermal component. In Figure 6, we show a histogram of X-ray burst spectra as a function of the blackbody contribution. The distribution clearly has two components, with a primary peak at $\approx 85\%$ and a secondary component at $\approx 65\%$. By calculating the average blackbody normalization of each histogram bin, we further see that the secondary component is associated with the PRE phase of bursts. Thus, during PRE, the

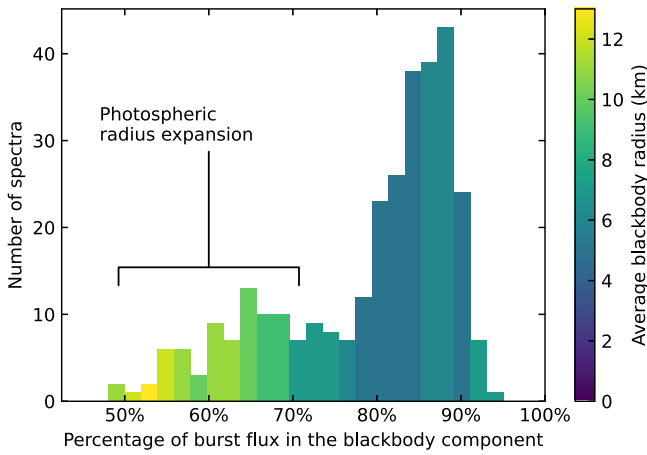


Figure 6. Histogram of the flux fraction contributed by the blackbody component. Each histogram bar is color coded according to the average blackbody normalization in that bin.

nonthermal emission accounts for $\approx 35\%$ of the total flux, while outside of the PRE phase, this contribution reduces to $\approx 15\%$. That the nonthermal flux contribution increases during the PRE phase suggests that whatever the scattering medium is, be it the disk or the boundary layer, it must be evolving under the influence of sustained irradiation by the burst emission. If so, we would expect the shape of the nonthermal emission to change over the course of an X-ray burst.

4.3. A Relation with Double-peaked Bursts

The shape of the bright bursts observed from 4U 1730–22 invites a comparison to double-peaked X-ray bursts. Such double-peaked bursts are characterized by a secondary peak in the bolometric X-ray flux that is astrophysical in origin (meaning that it is not due to the blackbody spectrum shifting out of the instrument passband). A number of models have been proposed to explain double-peaked X-ray bursts, including waiting points in the rp process (Fisker et al. 2004, 2008), stalled flame spreading (Bhattacharyya & Strohmayer 2006), remixing of unburned material (Keek et al. 2017), and line-of-sight absorption (Kajava et al. 2017).

Although the bursts of 4U 1730–22 do not show a secondary increase in bolometric flux, they do show a shoulder in their flux evolution. We can speculate that the process causing the flux to temporarily form a plateau may be (in part) the same process behind the second peak in other bursters. Indeed, the time-resolved spectroscopy of the bright bursts from 4U 1730–22 appears to be very similar to that of a double-peaked burst from 4U 1608–52 observed with NICER (Jaisawal et al. 2019), lending some support to this assumption.

Phenomenologically, one can imagine that the difference between observing a plateau and a secondary flux increase is simply one of the relative timescales for the PRE phase (what we called the “fast” component) and the rise time of the weak bursts (what we called the “slow” component). That is, if the PRE phase is faster than the slow rise, one sees a clear secondary peak (see, e.g., Li et al. 2021). If these two timescales are roughly similar (as is the case here), one sees a shoulder in the light curve. Finally, when the PRE phase lasts longer than the slow rise, one might see a break in the burst tail (e.g., burst 10). If these phenomena are indeed related, that would support the rp-process waiting point model, as it suggests that the

secondary peaks are at least partially due to a separation of the hydrogen and helium burning processes.

In this context, one might also ask if other X-ray bursters exhibit behavior similar to what we observe in 4U 1730–22. Indeed, the type of shoulders we find in the bright bursts are also seen in the profiles of prominent bursters such as 4U 1636–536 and Aql X-1 (Galloway et al. 2008; Güver et al. 2022a, 2022b) and have been previously attributed to the rp process (in’t Zand et al. 2017). Interestingly, these two bursters also show weak bursts that appear to have a similar (if much less pronounced) alignment to the cooling tails of their brighter counterparts (see, e.g., Güver et al. 2022a). Additional similarities between these sources exist; like 4U 1730–22, both 4U 1636–536 and Aql X-1 have high (>500 Hz) spin frequencies (Strohmayer et al. 1998; Zhang et al. 1998; Casella et al. 2008) and are known to show millihertz QPOs (Revnivtsev et al. 2001). On the other hand, Swift J1858.60814 is another example of an X-ray burster that shows both millihertz QPOs and very similar (bright) X-ray burst profiles (Buisson et al. 2020), yet there, the shoulder appears at different intensities for different X-ray bursts. Hence, physical processes beyond what we consider in this paper may be in play. A detailed comparison of these various sources is beyond the scope of this work but may make for an interesting topic of future investigation.

5. Conclusion

We have presented a spectroscopic analysis of 17 thermonuclear X-ray bursts observed from the neutron star X-ray transient 4U 1730–22. We observed PRE in 12 of these X-ray bursts, allowing us to estimate the source distance at 6.9 ± 0.2 kpc with an additional systematic uncertainty of 0.5 kpc.

We found that 4U 1730–22 shows both weak and bright bursts, and that these two types have a striking visual alignment: the bright bursts show a shoulder in their profile at the time that the weak bursts reach peak intensity. We suggest that this alignment points to two mostly independent nuclear burning processes: helium burning powering the bright PRE phase and rp-capture hydrogen burning setting the slower (and weaker) cooling tails.









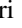


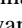


Although multiple interpretations might explain why both bright and weak bursts are observed from this source, we found that the burst properties could be naturally explained if we assume that accretion onto the neutron star proceeds through a boundary layer, such that accreted matter burns stably at the stellar equator, while unstable ignition occurs at higher latitudes.

This work made use of data and software provided by the High Energy Astrophysics Science Archive Research Center (HEASARC). P.B. acknowledges support from NASA through the Astrophysics Data Analysis Program (80NSSC20K0288) and the CRESST II cooperative agreement (80GSFC21M0002). G.C.M. was partially supported by Proyecto de Investigación Plurianual (PIP) 0113 (Nacional de Investigaciones Científicas y Técnicas, CONICET) and PICT-2017-2865 (Agencia Nacional de Promoción Científica y Tecnológica, ANPCyT). D.A. acknowledges support from the Royal Society. S.G. acknowledges the support of the CNES.

Facilities: ADS, HEASARC, NICER.

Software: heasoft (v6.30), nicerdas (v9).

ORCID iDs

Peter Bult  <https://orcid.org/0000-0002-7252-0991>
 Giulio C. Mancuso  <https://orcid.org/0000-0001-9822-6937>
 Tod E. Strohmayer  <https://orcid.org/0000-0001-7681-5845>
 Arianna C. Albayati  <https://orcid.org/0000-0001-5472-0554>
 Diego Altamirano  <https://orcid.org/0000-0002-3422-0074>
 Douglas J. K. Buisson  <https://orcid.org/0000-0002-5341-6929>
 Jérôme Chenevez  <https://orcid.org/0000-0002-4397-8370>
 Sebastien Guillot  <https://orcid.org/0000-0002-6449-106X>
 Tolga Güver  <https://orcid.org/0000-0002-3531-9842>
 Wataru Iwakiri  <https://orcid.org/0000-0002-0207-9010>
 Gaurava K. Jaisawal  <https://orcid.org/0000-0002-6789-2723>
 Mason Ng  <https://orcid.org/0000-0002-0940-6563>
 Andrea Sanna  <https://orcid.org/0000-0002-0118-2649>
 Jean H. Swank  <https://orcid.org/0000-0001-7079-9338>

References

- Altamirano, D., van der Klis, M., Wijnands, R., & Cumming, A. 2008, *ApJL*, **673**, L35
- Arnaud, K. A. 1996, in ASP Conf. Ser. 101, *Astronomical Data Analysis Software and Systems V*, ed. G. H. Jacoby & J. Barnes (San Francisco, CA: ASP), 17
- Ballantyne, D. R. 2004, *MNRAS*, **351**, 57
- Ballantyne, D. R., & Strohmayer, T. E. 2004, *ApJL*, **602**, L105
- Bhattacharyya, S., & Strohmayer, T. E. 2006, *ApJL*, **636**, L121
- Bhattacharyya, S., Yadav, J. S., Sridhar, N., et al. 2018, *ApJ*, **860**, 88
- Bilous, A. V., & Watts, A. L. 2019, *ApJS*, **245**, 19
- Boirin, L., Keek, L., Mendez, M., et al. 2007, *A&A*, **465**, 559
- Buisson, D. J. K., Altamirano, D., Bult, P., et al. 2020, *MNRAS*, **499**, 793
- Bult, P., Chakrabarty, D., Arzoumanian, Z., et al. 2020, *ApJ*, **898**, 38
- Bult, P., Jaisawal, G. K., Güver, T., et al. 2019, *ApJL*, **885**, L1
- Bult, P. M., Jaisawal, G. K., Joadand, A., et al. 2021, *ATel*, **14769**, 1
- Casella, P., Altamirano, D., Patruno, A., Wijnands, R., & van der Klis, M. 2008, *ApJL*, **674**, L41
- Cavecchi, Y., Galloway, D. K., Goodwin, A. J., Johnston, Z., & Heger, A. 2020, *MNRAS*, **499**, 2148
- Cavecchi, Y., Watts, A. L., & Galloway, D. K. 2017, *ApJ*, **851**, 1
- Chen, W., Shrader, C. R., & Livio, M. 1997, *ApJ*, **491**, 312
- Chen, Y. P., Zhang, S., Zhang, S. N., et al. 2019, *JHEAp*, **24**, 23
- Cominsky, L., Jones, C., Forman, W., & Tananbaum, H. 1978, *ApJ*, **224**, 46
- Cooper, R. L., & Narayan, R. 2007, *ApJL*, **657**, L29
- Cornelisse, R., in't Zand, J. J. M., Verbunt, F., et al. 2003, *A&A*, **405**, 1033
- Degenaar, N., Ballantyne, D. R., Belloni, T., et al. 2018, *SSRv*, **214**, 15
- Fisker, J. L., Schatz, H., & Thielemann, F.-K. 2008, *ApJS*, **174**, 261
- Fisker, J. L., Thielemann, F.-K., & Wiescher, M. 2004, *ApJL*, **608**, L61
- Fragile, P. C., Ballantyne, D. R., & Blankenship, A. 2020, *NatAs*, **4**, 541
- Fujimoto, M. Y., Hanawa, T., & Miyaji, S. 1981, *ApJ*, **247**, 267
- Galloway, D. K., in't Zand, J., Chenevez, J., et al. 2020, *ApJS*, **249**, 32
- Galloway, D. K., in't Zand, J. J. M., Chenevez, J., et al. 2018, *ApJL*, **857**, L24
- Galloway, D. K., & Keek, L. 2021, in *Timing Neutron Stars: Pulsations, Oscillations and Explosions*, ed. T. M. Belloni, M. Méndez, & C. Zhang (Berlin: Springer), 209
- Galloway, D. K., Muno, M. P., Hartman, J. M., Psaltis, D., & Chakrabarty, D. 2008, *ApJS*, **179**, 360
- Gottwald, M., Haberl, F., Parmar, A. N., & White, N. E. 1986, *ApJ*, **308**, 213
- Güver, T., Bostancı, Z. F., Boztepe, T., et al. 2022a, *ApJ*, **935**, 154
- Güver, T., Boztepe, T., Ballantyne, D. R., et al. 2022b, *MNRAS*, **510**, 1577
- Heger, A., Cumming, A., & Woosley, S. E. 2007, *ApJ*, **665**, 1311
- in't Zand, J. J. M., Visser, M. E. B., Galloway, D. K., et al. 2017, *A&A*, **606**, A130
- Inogamov, N. A., & Sunyaev, R. A. 1999, *AstL*, **25**, 269
- Iwakiri, W., Negoro, H., Nakajima, M., et al. 2021, *ATel*, **14757**, 1
- Jaisawal, G. K., Chenevez, J., Bult, P., et al. 2019, *ApJ*, **883**, 61
- Kaastra, J. S., & Bleeker, J. A. M. 2016, *A&A*, **587**, A151
- Kajava, J. J. E., Nättälä, J., Latvala, O.-M., et al. 2014, *MNRAS*, **445**, 4218
- Kajava, J. J. E., Sánchez-Fernández, C., Kuulkers, E., & Poutanen, J. 2017, *A&A*, **599**, A89
- Kashyap, U., Ram, B., Güver, T., & Chakraborty, M. 2022, *MNRAS*, **509**, 3989
- Keek, L., Arzoumanian, Z., Bult, P., et al. 2018a, *ApJL*, **855**, L4
- Keek, L., Arzoumanian, Z., Chakrabarty, D., et al. 2018b, *ApJL*, **856**, L37
- Keek, L., Galloway, D. K., in't Zand, J. J. M., & Heger, A. 2010, *ApJ*, **718**, 292
- Keek, L., Iwakiri, W., Serino, M., et al. 2017, *ApJ*, **836**, 111
- Kennea, J. A., Bahramian, A., Evans, P. A., et al. 2021a, *ATel*, **14686**, 1
- Kennea, J. A., Evans, P. A., Bahramian, A., et al. 2021b, *ATel*, **14688**, 1
- Kobayashi, K., Negoro, H., Serino, M., et al. 2021, *ATel*, **14683**, 1
- Koljonen, K. I. I., Kajava, J. J. E., & Kuulkers, E. 2016, *ApJ*, **829**, 91
- Kuulkers, E., den Hartog, P. R., in't Zand, J. J. M., et al. 2003, *A&A*, **399**, 663
- Lampe, N., Heger, A., & Galloway, D. K. 2016, *ApJ*, **819**, 46
- Li, C., Zhang, G., Méndez, M., Wang, J., & Lyu, M. 2021, *MNRAS*, **501**, 168
- Li, Z., Yu, W., Lu, Y., Pan, Y., & Falanga, M. 2022, *ApJ*, **935**, 123
- London, R. A., Howard, W. M., & Taam, R. E. 1986, *ApJ*, **306**, 170
- Madej, J., Joss, P. C., & Różańska, A. 2004, *ApJ*, **602**, 904
- Makishima, K., Maejima, Y., Mitsuda, K., et al. 1986, *ApJ*, **308**, 635
- Maurer, I., & Watts, A. L. 2008, *MNRAS*, **383**, 387
- Mitsuda, K., Inoue, H., Koyama, K., et al. 1984, *PASJ*, **36**, 741
- Narayan, R., & Heyl, J. S. 2003, *ApJ*, **599**, 419
- Negoro, H., Kohama, M., Serino, M., et al. 2016, *PASJ*, **68**, S1
- Remillard, R. A., Loewenstein, M., Steiner, J. F., et al. 2022, *AJ*, **163**, 130
- Revnivtsev, M., Churazov, E., Gilfanov, M., & Sunyaev, R. 2001, *A&A*, **372**, L38
- Roy, P., Beri, A., & Bhattacharyya, S. 2021, *MNRAS*, **508**, 2123
- Russell, D. M., Baglio, M. C., Saikia, P., Abdelmaguid, M., & Lewis, F. 2021, *ATel*, **14693**, 1
- Schatz, H., Aprahamian, A., Barnard, V., et al. 2001, *PhRvL*, **86**, 3471
- Spitkovsky, A., Levin, Y., & Ushomirsky, G. 2002, *ApJ*, **566**, 1018
- Strader, J., Sokolovsky, K., Aydi, E., et al. 2021, *ATel*, **14694**, 1
- Strohmayer, T. E., Zhang, W., Swank, J. H., White, N. E., & Lapidus, I. 1998, *ApJL*, **498**, L135
- Suleimanov, V., Poutanen, J., Revnivtsev, M., & Werner, K. 2011, *ApJ*, **742**, 122
- Suleimanov, V. F., Poutanen, J., Nättälä, J., et al. 2017, *MNRAS*, **466**, 906
- Tomsick, J. A., Gelino, D. M., & Kaaret, P. 2007, *ApJ*, **663**, 461
- van Paradijs, J., & White, N. 1995, *ApJL*, **447**, L33
- Walker, M. A. 1992, *ApJ*, **385**, 642
- Walker, M. A., & Meszaros, P. 1989, *ApJ*, **346**, 844
- Wallace, R. K., & Woosley, S. E. 1981, *ApJS*, **45**, 389
- Watts, A. L. 2012, *ARA&A*, **50**, 609
- Wilms, J., Allen, A., & McCray, R. 2000, *ApJ*, **542**, 914
- Worpel, H., Galloway, D. K., & Price, D. J. 2013, *ApJ*, **772**, 94
- Worpel, H., Galloway, D. K., & Price, D. J. 2015, *ApJ*, **801**, 60
- Zdziarski, A. A., Johnson, W. N., & Magdziarz, P. 1996, *MNRAS*, **283**, 193
- Zhang, W., Jahoda, K., Kelley, R. L., et al. 1998, *ApJL*, **495**, L9
- Życki, P. T., Done, C., & Smith, D. A. 1999, *MNRAS*, **309**, 561